

# Structural, Electronic, and Vibrational Properties of the Ti–O–Ti Quantum Wires in the Titanosilicate ETS-10

Alessandro Damin,<sup>†</sup> Francesc X. Llabrés i Xamena,<sup>†,‡</sup> Carlo Lamberti,<sup>†,‡,§</sup>  
Bartolomeo Civalieri,<sup>†</sup> Claudio M. Zicovich-Wilson,<sup>#</sup> and Adriano Zecchina<sup>\*,†,‡,§</sup>

Dipartimento di Chimica IFM, Università di Torino, Via P. Giuria 7, I-10125 Torino, Italy,  
INSTM UdR Torino Università, INFN UdR Torino Università, and Facultad de Ciencias,  
Universidad Autónoma del Estado de Morelos, Av. Universidad 1001, Col. Chamilpa,  
62210 Cuernavaca (Morelos), Mexico

Received: September 29, 2003

The periodic *ab initio* CRYSTAL code approach has been adopted to perform for the first time the calculation of the vibrational frequencies of the titanosilicate ETS-10, modeled by one-dimensional periodic chains (including positive counterions). The cell parameter and the internal atomic coordinates of the models have been fully optimized at the Hartree–Fock (HF) level imposing a  $P2_1/m11$  symmetry. The so-obtained geometries well agree with the experimental data coming from single-crystal X-ray diffraction experiments. The HF and B3LYP band gaps (the latter evaluated at the HF geometry) are 14.03 and 5.22 eV, respectively. The analysis of the density of states at both HF and B3LYP levels shows that states coming from the apical oxygen atoms of the  $\text{TiO}_6$  octahedra are quite confined in a narrow range of energy. Frequencies have been calculated at HF level. The analysis of the obtained normal modes assigns the Raman “725”  $\text{cm}^{-1}$  fingerprint of ETS-10 to a total-symmetric combination of the Ti–O bond stretching involving only the apical oxygen atoms. The analysis of the vibrational modes of fragments of increasing size indicates that, for this mode to be present, the chain of corner-sharing  $\text{TiO}_6$  octahedra has to be confined in a siliceous matrix.

## 1. Introduction

The titanosilicate ETS-10 is a microporous material formed by corner-sharing  $\text{TiO}_6$  octahedra and  $\text{SiO}_4$  tetrahedra linked through bridging oxygen atoms. Each titanium atom incorporates a net negative charge of  $-2$  that is compensated by extraframework charge-balancing cations ( $\text{Na}^+$  and  $\text{K}^+$  in the as-synthesized material).<sup>1</sup> The layout of structural units generates a three-dimensional interconnected system of 12-membered  $\text{SiO}_4$  ring channels with free openings of about  $8 \text{ \AA} \times 5 \text{ \AA}$  in diameter, as illustrated in Figure 1a. These structural channels are straight in the [100] and [010] directions and tortuous along the [001] direction.

ETS-10 can exist as two *ideal* polymorphs that differ in the stacking sequence along the [001] direction. In polymorph A (tetragonal system, space group  $P4_1$  or  $P4_3$ ) zigzag channels in the  $c$  direction are present, while in polymorph B (monoclinic system, space group  $C2/c$ ), they are diagonally arranged. The *real* ETS-10 is actually a virtually random intergrowth of both polymorphs, which results in a disordered material containing stacking faults and line defects. Because of this inherent disorder, the resolution of the structure of ETS-10 has been particularly challenging. A first structural model was proposed by Anderson et al.<sup>2,3</sup> from a combination of electron microscopy, X-ray powder diffraction (XRPD) and electron diffraction, solid-state NMR, and molecular modeling. The structure proposed

by those authors was later confirmed by Wang and Jacobson using single-crystal diffraction.<sup>4</sup>

Besides its great exchange capacity toward divalent cations,<sup>5</sup> one of the most striking features of ETS-10 is that the  $\text{TiO}_6$  octahedra form linear chains running in two perpendicular directions of the crystal and being isolated from one another by the siliceous matrix. This results in the generation of one-dimensionally confined atomic Ti–O–Ti–O–Ti wires,<sup>6–8</sup> that give rise to the peculiar optical and electronic properties of the material. Indeed, ETS-10 is a semiconductor material with a band gap of about 4 eV. Semiconducting quantum wires are being actively investigated because of their great potential in several areas of optoelectronics.<sup>9–12</sup> From this point of view, the titanosilicate ETS-10 is an interesting material because it directly contains well-defined quantum wires in its crystalline structure. This provides an unprecedented well-defined model system in which to study quantum wire properties.

The quantum wires can behave as antenna-like systems, that allow harvesting light and transporting it to the external defects (like chain terminations emerging at the external surfaces) or chain truncations (internal defects). This confers to ETS-10 a photocatalytic activity similar to that of  $\text{TiO}_2$ . Indeed, the activity of ETS-10 in photocatalysis has been known for a few years.<sup>13–17</sup> Most interestingly and in contrast with other bulk metal oxide semiconductors (such as  $\text{TiO}_2$ ), the material presents shape-selective properties. This has been recently demonstrated for the photodegradation of aromatic molecules of different size: the molecules that, by virtue of their small size, can enter the channels of ETS-10 are protected from photodegradation, which occurs only at the external surface.<sup>14,16</sup>

All of the optic and electronic properties of ETS-10 commented above are directly related to the local structure of the

\* To whom correspondence should be addressed. E-mail: [adriano.zecchina@unito.it](mailto:adriano.zecchina@unito.it).

<sup>†</sup> Dipartimento di Chimica IFM, Università di Torino.

<sup>‡</sup> INSTM Unità di Torino Università.

<sup>§</sup> INFN Unità di Torino Università.

<sup>#</sup> Departamento de Física, Universidad Autónoma del Estado de Morelos.

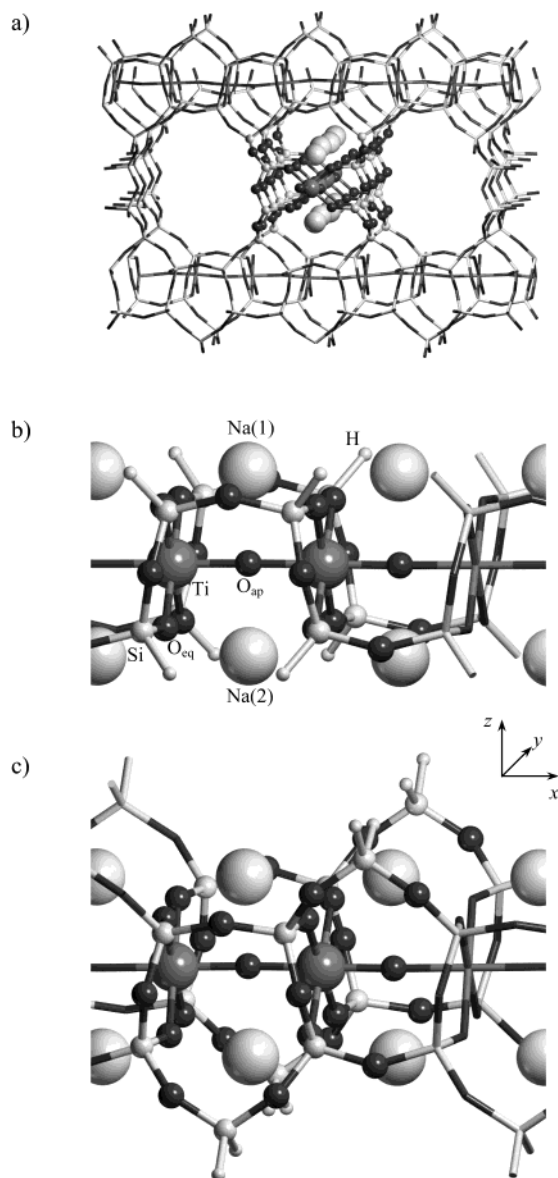


**Figure 1.** Layout of structural units (a) of ETS-10. The fragment of the framework included in the optimized models I and II is highlighted. Part b shows model I; part c shows model II. In parts b and c, the atoms of the unit cell are highlighted.

Ti—O—Ti—O—Ti wires. Indeed, it has been pointed out that the siliceous matrix surrounding these chains has the only effect of providing an insulating medium for them and that the final optical properties of the material are not affected by ionic exchange or by the presence of adsorbates in the structural channels.<sup>6,7</sup> This means that the Ti—O—Ti chains are actually isolated from the surroundings (unless (point) defects leading to exposed titanium sites are present). In fact, the very crude model of a particle in a monodimensional cylindrical box of a diameter fixed by the  $O_{eq}$ —Ti— $O_{eq}$  unit (ca. 0.4 nm) was able to reproduce the ETS-10 band gap (4.02 eV) by adding to the  $E_g$  of  $TiO_2$  the expected blue shift due to the confinement effect.<sup>6,7</sup> The accuracy of the prediction, obtained with such a simple method, is because the optical properties of the material are dictated by the Ti—O—Ti wires only, its three-dimensional structure playing a negligible role.

Among the different experimental techniques that have been used in the characterization of ETS-10, Raman spectroscopy has proven to be very useful for the study of the local structure around the titanium ions. Su et al.<sup>18</sup> have recently presented a

systematic Raman study on several titanosilicates, in which titanium was present in different coordination. They pointed out that the presence of an intense Raman band around  $750\text{ cm}^{-1}$  was exclusive of materials having Ti—O—Ti linkages in corner-sharing  $TiO_6$  chains, such as those present in ETS-10 (Raman band at ca.  $725\text{ cm}^{-1}$  with a tail in the high-frequency side). Moreover, it has been recently pointed out<sup>19,20</sup> that the exact position and broadness of this Raman active band in ETS-10 is very sensitive to the average length of the Ti—O—Ti chains (and, thus, to the concentration of defects in the structure). Although it is well stated that this Raman band is associated with a Ti—O stretch, it is still not so clear whether it is a stretching mode localized along the chain (involving only the axial oxygens) or the equatorial oxygens are also participating (thus being a breathing mode of the  $TiO_6$  octahedra).

Only a limited number of computational works on ETS-10 based on ab initio techniques are present in the literature. In the work of de Man and Sauer,<sup>21</sup> a simplified cluster model was used for the simulation of the Ti octahedron in ETS-10: it consisted of a central titanium atom with two water molecules in axial positions to mimic the apical oxygens of the octahedron ( $O_{ap}$ ) and contained the three-membered rings including the central Ti atom and its four equatorial oxygens ( $O_{eq}$ ). This model was optimized at Hartree—Fock level, giving final Ti— $O_{eq}$  distances of 1.87 Å and two longer Ti— $O_{ap}$  distances of 2.15 Å.

In the works of Ching et al.<sup>22</sup> and of Bordiga et al.,<sup>8</sup> a periodic approach was adopted. In ref 22, the authors used the internal coordinates of polymorph B (derived from X-ray powder diffraction by Anderson et al.)<sup>2,3</sup> and optimized only the positions of the extraframework ( $Na^+$ ) cations using a local-density approximation (LDA) Hamiltonian. They found that the most stable position for the charge-balancing (monovalent) cations was in correspondence with the apical oxygen and coordinated to four equatorial oxygens (two  $O_{eq}$  from every neighboring  $TiO_6$  octahedron), giving rise to Na—O distances ranging from 1.87 to 2.37 Å. These authors also presented an analysis of the electronic structure of ETS-10, showing that the states close to the top of the valence band (VB) are mainly composed of the 2p orbitals of  $O_{eq}$  and  $O_{ap}$  atoms, while the states of the bottom of the conduction band (CB) are mainly composed of the 3d orbitals of Ti. The band gap evaluated as the difference between the top of the VB and the bottom of the CB was 2.33 eV, clearly underestimated with respect to the experimental value of 4.02 eV.<sup>6,7</sup>

On this basis, in a later work of Bordiga et al.,<sup>8</sup> a simplified model of ETS-10 was adopted. It consisted of a three-dimensional array of parallel Ti—O—Ti wires separated by the same distance found in the real crystal and included the first shell of silicon atoms around the central titanium. Silicon dangling bonds were capped with OH groups, and positive counterions were not included, which resulted in an electron-deficient system. The authors performed energy calculations at LDA level (without optimizing the internal coordinates), obtaining the electronic structure of the system. The analysis of the densities of states (DOSs) showed that the model resulted to be metallic with the Fermi level located inside the VB. This result is in clear contradiction with the semiconducting character of ETS-10.<sup>6,7</sup> As recognized by the authors of ref 8, the presence of holes in the VB was due to the absence of Na atoms in the investigated model.

To the best of our knowledge, no theoretical works have been devoted up to now to the analysis of the vibrational features of ETS-10. Following the idea proposed in ref 8, we have adopted

an ab initio periodic approach as implemented in the CRYSTAL code<sup>23</sup> on simplified monodimensional models of ETS-10, including the central Ti–O–Ti rod and the surrounding silicon atoms (see Figure 1, parts b and c) and including also the Na<sup>+</sup> counterions. The equilibrium positions of all of the atoms in the models have been optimized by means of analytical gradient calculation. This represents a strong improvement with respect to what was done in refs 8 and 22. The geometric, vibrational, and electronic properties derived from ETS-10 optimized models will be presented for the first time, and the results obtained will be compared to those obtained experimentally.

## 2. Models and Computational Details Section

**2.1. Models.** The models (I and II) adopted in the present study are shown in Figure 1 (parts b and c, respectively); basically, they reproduce the structural unit of ETS-10, as shown by their comparison with part a of Figure 1. Model I is very similar to the model employed in ref 8, where a tridimensional array of ETS-10 structural units was adopted; however, in the present models, positive counterions (Na<sup>+</sup>) are also included. Notice that our models should reproduce more closely a (Na,Ns)-ETS-10, rather than the commercial (Na,K)-ETS-10, which has been used in the past for spectroscopic studies. The Na<sup>+</sup> ions are located near the O<sub>ap</sub> atoms on each side of the *xy* plane. Due to the alternating position (up and down) of the silicon atoms, there are two nonequivalent Na<sup>+</sup> positions, namely, Na(1) and Na(2). This holds also for model II, which includes the silicon atoms completing the five-membered rings surrounding the Ti–O–Ti chains, which are well visible in part a of Figure 1.

Both models are obtained from a periodic monodimensional (the *a* cell parameter has to be optimized) repetition of the unit cell highlighted in parts b and c of Figure 1, which contain 40 (model I) and 52 (model II) atoms. The unit cell has a *P*<sub>21</sub>/*m*11 symmetry in both models, leading to 13 (TiO<sub>6</sub>Si<sub>2</sub>H<sub>2</sub>Na<sub>2</sub>) and 19 (TiO<sub>8</sub>Si<sub>4</sub>H<sub>4</sub>Na<sub>2</sub>) irreducible atoms in the asymmetric unit, respectively. At variance with respect to ref 8, where Si dangling bonds were capped by hydroxyl groups, in the present study H atoms are used. In both models, the two O<sub>ap</sub> atoms are equivalent; the eight O<sub>eq</sub> atoms are split in two nonequivalent sets of four symmetry-related O<sub>eq</sub>. Finally for symmetry reasons, all of the Ti–O<sub>ap</sub> must be equivalent, and only displacements along the *y* and *z* directions will be allowed during the optimization of the internal coordinates.

The use of the *P*<sub>21</sub>/*m*11 symmetry has been justified on the basis of a preliminary optimization cycles (vide infra section 2.2 for further details) on model II without symmetry constraints, see Table 1. Even by starting from deformed initial coordinates (O<sub>ap</sub>–Ti(1)–O<sub>ap</sub>–Ti(2)–O<sub>ap</sub>, geometry along the chain), the optimized structure results in two equivalent Ti atoms. In particular, Ti–O<sub>ap</sub> are equivalent within 0.001 Å, reflecting a single Ti–O distance along the chain. The same holds for the Ti–O<sub>eq</sub> distances. The analysis of the eight O<sub>eq</sub>–Ti–O<sub>ap</sub> (four in *P*<sub>21</sub>/*m*11 symmetry) angles, equivalent to 90° within 0.5°, and of the eight O<sub>eq</sub>–Ti–O<sub>eq</sub> angles, within 83° and 97°, implies that we are dealing with rigid octahedral TiO<sub>6</sub> units deformed in the equatorial plane and slightly rotated around the *z* axis, as witnessed by the Ti(1)–O<sub>ap</sub>–Ti(2) angle significantly different from 180°.

**2.2. Computational Details.** Models I and II have been fully optimized at the Hartree–Fock (HF) level by adopting an upgraded version of the CRYSTAL-98 code<sup>23</sup> that allows the optimization of the atomic coordinates with fixed cell parameters, by employing a modified conjugate gradient algorithm

**TABLE 1: Selected Geometric Features of Optimized Model II in *P*<sub>1</sub> Symmetry<sup>a</sup>**

	model II ( <i>P</i> <sub>1</sub> )
<i>a</i>	7.5172
Ti(1)–O <sub>ap</sub>	1.880/1.889
Ti(2)–O <sub>ap</sub>	1.880/1.888
Ti(1)–O <sub>eq</sub>	2.000/1.999/1.997/2.001
Ti(2)–O <sub>eq</sub>	2.000/2.000/1.998/2.000
Ti(1)–O <sub>ap</sub> –Ti(2)	171.5
O <sub>ap</sub> –Ti(1)–O <sub>ap</sub>	179.8
O <sub>ap</sub> –Ti(2)–O <sub>ap</sub>	179.8
O <sub>eq</sub> –Ti(1)–O <sub>eq</sub>	83.2/83.5/96.5/96.7
O <sub>eq</sub> –Ti(2)–O <sub>eq</sub>	83.2/83.5/96.6/96.7
O <sub>eq</sub> –Ti(1)–O <sub>ap</sub>	89.5/90.4
O <sub>eq</sub> –Ti(2)–O <sub>ap</sub>	89.5/90.4

<sup>a</sup> Ti(1) and Ti(2) are the two nonequivalent Ti atoms in the unit cell. Since the optimized geometry lead to a higher symmetry (*P*<sub>21</sub>/*m*11), only the geometry of the TiO<sub>6</sub> moiety is reported here for the sake of brevity. The reader should refer to Table 2 for the higher shell structure around Ti. The *a* cell parameter and the distances in the table are expressed in Å and the angles are expressed in deg.

as proposed by Schlegel.<sup>24</sup> In this scheme, the energy gradients with respect to the atomic positions are computed analytically, and convergence is tested on the root-mean-square (RMS) and the absolute value of the largest component of both the gradients and the estimated displacement of nuclei. In the present calculations, the threshold for the maximum and the RMS forces and the maximum and the RMS atomic displacements on all atoms have been set to (in au) 0.000 45, 0.000 30 and 0.001 80, 0.001 20, respectively. The accuracy of the code in the simulation of the structural properties of titanosilicate systems has been recently tested in a titanium–chabazite material.<sup>25</sup> The *a* cell parameter has been optimized by adopting a cyclic procedure, alternating (i) the optimization of the atomic positions (analytical gradient) and (ii) the optimization of the *a* cell parameter (numerical gradient evaluation). For the sake of brevity, the full details of the whole procedure, which is performed maintaining the *P*<sub>21</sub>/*m*11 symmetry, are included as Supporting Information. The final HF optimized structures of models I and II have been employed as input structures for (i) single-point calculations (two *k* points along the *a* direction) at both HF and B3LYP<sup>26,27</sup> level to analyze the electronic structure, which will be presented in density of states (DOS) plots (computed adopting eight *k* points along the *a* direction) and (ii) calculations (HF level) of the harmonic vibrational frequencies (a detailed description of such calculation is included as Supporting Information) and the symmetry analysis of the associated normal modes. Computational parameters have been set<sup>23a</sup> at TOLINTEG = 7 7 7 7 14 (two *k* points along the *a* direction) and convergence criteria in the SCF cycle of 10<sup>–10</sup> hartree.

Finally, the atom-centered Gaussian basis set employed in all calculations can be summarized as follows: (a) For the Ti atom,<sup>28</sup> 8/6411/31G (s/sp/d, respectively) contraction. Outermost  $\zeta_{sp} = 0.324$  bohr<sup>–2</sup> and  $\zeta_d = 0.230$  bohr<sup>–2</sup>. (b) For the Si atom,<sup>28</sup> 6/621/1G (s/sp/d) contraction. Outermost  $\zeta_{sp} = 0.130$  bohr<sup>–2</sup> and  $\zeta_d = 0.500$  bohr<sup>–2</sup>. (c) For the O atom,<sup>28</sup> 6/31/1G (s/sp/d) contraction. Outermost  $\zeta_{sp} = 0.274$  bohr<sup>–2</sup> and  $\zeta_d = 0.600$  bohr<sup>–2</sup>. (d) For the H atom, 3/1/1G (s/s/p) contraction. Outermost  $\zeta_s = 0.161$  bohr<sup>–2</sup>. (e) For the Na atom,<sup>29</sup> 8/5/1/1G (s/sp/sp/sp) contraction. Outermost  $\zeta_{sp} = 0.323$  bohr<sup>–2</sup>.

## 3. Results and Discussion

**3.1. Optimized Models.** As previously described in the Computational Details section, the *a* cell parameter and internal coordinates of both model I and II (see Figure 1) have been



**TABLE 2: Selected Geometric Features of  $P2_1/m11$  Optimized Models I and II, Together with Geometries Obtained from Single-Crystal X-ray Measurements<sup>a</sup>**

	model I ( $P2_1/m11$ )	model II ( $P2_1/m11$ )	experimental
$a$	7.5156	7.5180	7.481(1)
Ti–O <sub>ap</sub>	1.879	1.883	1.872(1)
Ti–O <sub>eq</sub>	2.004/2.003	2.000/1.999	1.99(1)
Si–O <sub>eq</sub>	1.615/1.615	1.611/1.611	1.61(1)
Na(1)–O <sup>b</sup>	2.44/2.44/2.28	2.47/2.42/2.31	2.57/2.57/2.63
Na(2)–O <sup>b</sup>	2.41/2.41/2.29	2.49/2.40/2.32	2.53/2.53/2.50
Ti–O <sub>ap</sub> –Ti	179.2	172.6	177.9
O <sub>ap</sub> –Ti–O <sub>ap</sub>	180.0	180.0	180.0
O <sub>eq</sub> –Ti–O <sub>eq</sub>	82.7/97.3	83.3/96.7	84.9/95.1
O <sub>eq</sub> –Ti–O <sub>ap</sub>	89.9/90.1	89.7/90.3	88.9/91.1

<sup>a</sup> Data are taken from ref 4. The value given for  $a$  is halved because it corresponds to a subcell of the true unit cell. The  $a$  cell parameter and the distances in the table are expressed in Å and the angles are expressed in deg. <sup>b</sup> The first two distances correspond to Na–O<sub>eq</sub> and the 3rd to Na–O<sub>ap</sub>.

fully optimized at HF level. The values obtained for  $a$  in the two models (7.5156 and 7.5180 Å, respectively) are in very good agreement with that determined experimentally<sup>4</sup> (7.481(1) Å, see Table 2). Of course, in our monodimensional models, the parameters  $b$  and  $c$  have no meaning. The two structures were found to be real local minima, as demonstrated by the absence of negative frequencies (vide infra, section 3.3). Selected geometrical features of the optimized structures are listed in Table 2, together with experimental results coming from single-crystal X-ray diffraction.<sup>4</sup> Both models I and II reproduce quite well the experimental geometry of the TiO<sub>6</sub> moiety and of the silicon atoms in the second coordination shell around titanium (see Table 2). In both models, the TiO<sub>6</sub> octahedra are slightly deformed in the equatorial plane, as testified by the two different values of O<sub>eq</sub>–Ti–O<sub>eq</sub> (smaller and bigger than 90°). The O<sub>ap</sub>–Ti–O<sub>eq</sub> angles (quite near to 90°) show that the Ti atom lies on the plane defined by the four O<sub>eq</sub> atoms. The Ti–O<sub>ap</sub> distances, which are equal by symmetry, change very slightly on passing from model I to model II and are in quite good agreement with the experimental value. The same can be observed for the Ti–O<sub>eq</sub> distances, which result longer than the Ti–O<sub>ap</sub> ones. Finally, the TiO<sub>6</sub> octahedron results slightly tilted in model II with respect to the  $x$  axis, as shown by the Ti–O<sub>ap</sub>–Ti angle, which differs from 180°. So, we can conclude that the TiO<sub>6</sub> moiety is constituted by slightly deformed octahedral units rigidly tilted around the  $z$  axis and having two identical Ti–O<sub>ap</sub> distances. From the experimental X-ray derived geometry, no ferroelectric distortion (displacement of Ti from the equatorial plane defined by O<sub>eq</sub>) seems to occur. Moreover, no alternating (short–long) Ti–O<sub>ap</sub> distances along the chain are present, in clear contrast with the model proposed in ref 30 on the basis of EXAFS data, where a short (1.7 Å) and a long (2.1 Å) Ti–O<sub>ap</sub> distance have been inferred. Some of us have performed EXAFS measurements on ETS-10, finding an experimental signal that is similar to that reported in ref 30. Although the model suggested in ref 30 gave an acceptable mathematical fitting of the experimental signal, it is noteworthy to say that also the use of the optimized structures of models I and II give a satisfactory agreement. The obtained results and discussion will be presented elsewhere.

Due to the imposed symmetry constraints in the optimization of the adopted models I and II, the above deformations cannot occur because the O<sub>ap</sub> distances are forced to be identical (the two O<sub>ap</sub> atoms are related by symmetry). To give some insights about this topic, we have also performed an additional optimiza-

tion of model II without symmetric constraints (cell with  $P1$  symmetry), starting from a structure in which the titanium was displaced outside the equatorial plane (thus giving rise to ferroelectric titanium centers and to alternating short and long Ti–O<sub>ap</sub> distances) and using the same optimization parameters as in the two previous models. The final optimized structure evolved to a situation essentially identical (compare Tables 1 and 2) to that obtained in our two models (i.e.,  $P2_1/m11$ ).

Finally, the equilibrium position of the Na<sup>+</sup> ions in the optimized structures are close to those found experimentally by Wang and Jacobson using single-crystal X-ray diffraction<sup>4</sup> and to those calculated by Ching et al.<sup>22</sup> and Grillo and Carrazza<sup>31</sup> using LDA and a combination of lattice energy minimization and Monte Carlo calculations, respectively. The Na<sup>+</sup> ions resulted to be (in both models) in 5-fold coordination with the four equatorial and one apical oxygen atoms at distances ranging from ca. 2.4 to 2.6 Å (see Table 2). In the real material, as already pointed out by Wang and Jacobson,<sup>4</sup> the Na<sup>+</sup> ions weakly interact with H<sub>2</sub>O, thus causing a slight elongation of the distances between the Na ions and the framework oxygens. This fact can easily explain the systematically slightly longer Na–O distances found by single-crystal X-ray diffraction with respect to those found in our optimized models (which do not account for the presence of water).

**3.2. Electronic Structure.** The electronic structure of model II has been analyzed through the densities of states (DOSs), both at HF (Figure 2) and B3LYP (Figure 3) levels. The latter has been obtained at the HF geometry.

In both cases (see parts a of Figures 2 and 3), the final electronic structure results in a fully occupied VB and an unoccupied CB separated by an energy gap ( $E_g$ , evaluated as the difference between the top of the VB and the bottom of the CB). The obtained  $E_g$  values are 14.03 (HF) and 5.22 eV (B3LYP); as expected, HF overestimates by a factor greater than three the experimental value (4.02 eV),<sup>6–8</sup> whereas B3LYP is much closer (+30%), in agreement with the trends observed in refs 32 and 33. Single-point calculations on the HF-optimized structure performed also at the LDA-VWN<sup>34,35</sup> level (results not shown for the sake of brevity) give an  $E_g$  of 3.22 eV, that is, smaller than the HF, B3LYP, and experimental ones. Therefore the expected trend for  $E_g$  (HF  $\gg$  B3LYP  $>$  LDA-VWN) is observed.

A detailed analysis of the top of VB and bottom of the CB is presented in parts b and c of Figures 2 and 3, in which the total DOSs and the contributions by the oxygen atoms and Ti are rendered. As far as the latter contribution, a qualitative similar picture emerges from both HF and B3LYP DOSs: Ti covers with 3d orbitals the major part of the bottom of CB and does not contribute appreciably to the top of the VB. This result suggests that upon thermal or photoexcitation of ETS-10, Ti<sup>4+</sup> is reduced to Ti<sup>3+</sup>. The top of VB, in both HF and B3LYP DOSs, receives mainly contributions from the oxygen atoms (although an important contribution by the capping H atoms can be observed in HF DOSs around –0.46 hartree). In both cases, two groups of states can be distinguished (V1 and V2) that are separated by a small gap of about 0.01 hartree (ca. 0.3 eV). The interesting point is that the V2 group of states is formed almost exclusively by states belonging to O<sub>eq</sub> and O<sub>ap</sub> atoms. Moreover, no states from the O<sub>ap</sub> atoms (i.e., oxygen atoms along the Ti–O–Ti–O–Ti chains) contribute to the V1 group (results not shown for the sake of clarity). A similar distribution of states is obtained at LDA-VWN level also. It comes out that states coming from O<sub>ap</sub> are confined in a narrow range of energies inside the V2 group of states (0.5–0.6 eV). Both

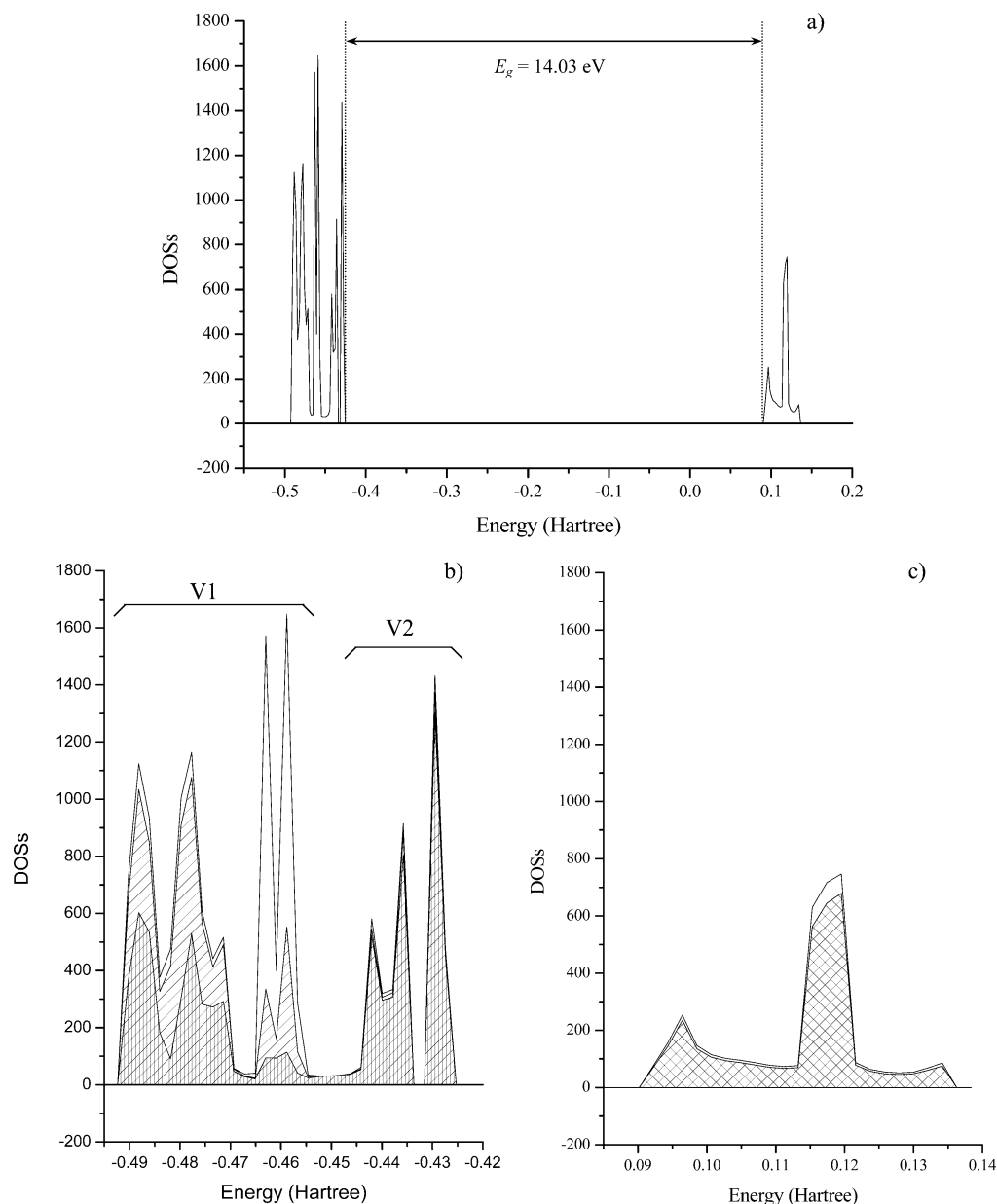


**Figure 2.** Densities of states (DOSs) computed on the model II optimized at RHF level: (a) total DOSs with the computed band gap ( $E_g$ ) indicated; (b) detail of the top of the valence band with the total DOSs and the corresponding contributions by the oxygen atoms rendered, respectively, by full line, sparse shading (all oxygen atoms), and dense shading (only oxygen atoms directly bonded to titanium); (c) detail of the bottom of the conduction band with the total DOSs and the contribution by the titanium ions represented by full line and shaded area, respectively.

considerations lead to the suggestion that a confinement of the electrons of the  $\text{TiO}_6$  octahedra exists. Therefore, the first electronic transition consists basically in a ligand (mainly  $\text{O}_{\text{eq}}$  and  $\text{O}_{\text{ap}}$ ) to metal (Ti) charge transfer of the type  $\text{O}^{2-}\text{Ti}^{4+} + h\nu \rightarrow \text{O}^-\text{Ti}^{3+}$ .

These results are in qualitative agreement with those obtained by Ching et al.<sup>22</sup> using LDA Hamiltonian and the whole cell of ETS-10, the main difference with the present results consisting in the  $E_g$  value (2.33 vs 3.22 eV) due to the one-dimensional model used in the present work.

**3.3. Vibrational Analysis.** The vibrational frequencies of models I and II have been calculated at the HF level. A comparison between the calculated Raman spectrum for model II and that obtained experimentally is shown in Figure 4. The experimental Raman spectrum is dominated by an intense band centered at  $725\text{ cm}^{-1}$ , in agreement with previous results from the literature.<sup>18–20</sup> In addition, a number of minor bands are observed with great detail. The discussion of these minor

features, however, falls beyond the scope of the present work, and they will be commented on elsewhere.<sup>36</sup> The  $725\text{ cm}^{-1}$  band has been considered as a fingerprint of ETS-10 and related to the presence of the  $\text{Ti}-\text{O}-\text{Ti}-\text{O}-\text{Ti}$  chains.<sup>18</sup>

In particular, the systematic Raman study on a set of titanasilicate model compounds (which structures are well-known from XRD) shows that the model requesting strong differences in the axial  $\text{Ti}-\text{O}$  distances is not compatible with the observation. In fact, in ref 18, it is unambiguously proven that the position of the  $725\text{ cm}^{-1}$  band is strongly affected by the distribution of the distances between Ti atoms and the oxygen atoms bridging corner-sharing  $\text{TiO}_6$  octahedra. In ref 18, two Raman spectra of two different titanosilicates, where isolated corner-sharing  $\text{TiO}_6$  octahedra chains are present, are taken into account and compared with the Raman spectrum of ETS-10. In the first case, the Raman spectrum of  $\text{Na}_2\text{TiSi}_4\text{O}_{11}$  has been analyzed; it presents an intense signal at  $764\text{ cm}^{-1}$ ; in this case, two distances characterize the  $\text{Ti}-\text{O}$  bonds along the

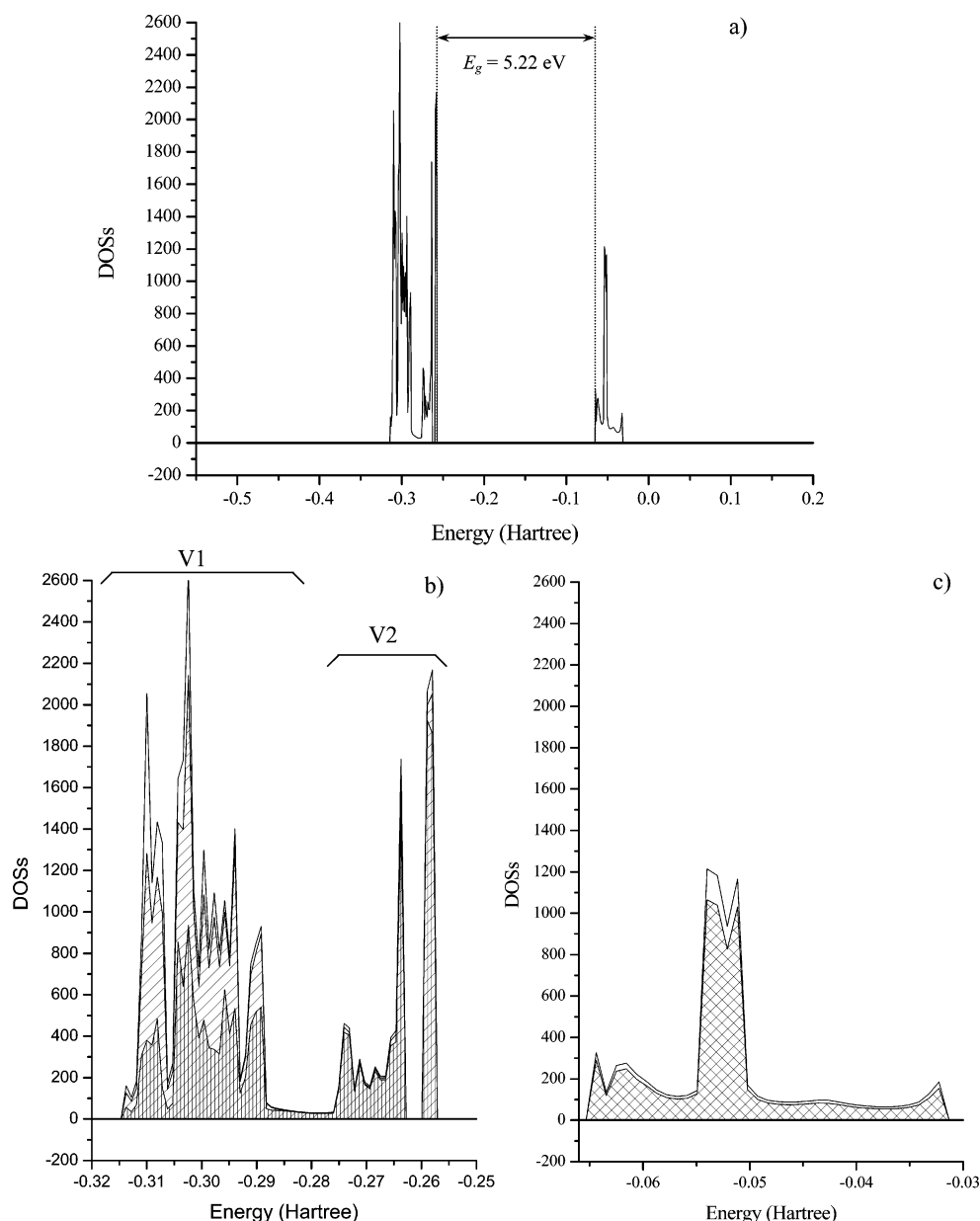


**Figure 3.** Densities of states (DOSs) computed at B3LYP level on the RHF optimized model II: (a) total DOSs with the computed band gap ( $E_g$ ) indicated; (b) detail of the top of the valence band with the total DOSs and the corresponding contributions by the oxygen atoms rendered, respectively, by full line, sparse shading (all oxygen atoms), and dense shading (only oxygen atoms directly bonded to titanium); (c) detail of the bottom of the conduction band with the total DOSs and the contribution by the titanium ions represented by full line and shaded area, respectively.

chain, that is, 1.90 and 2.07 Å, the sequence being (Ti—O—Ti—O—Ti—O—Ti). In the second case, the Raman spectrum of  $\text{CaTiSiO}_5$  has been analyzed; in this case, no signal around 725  $\text{cm}^{-1}$  has been observed, the most intense peak being now located at 611  $\text{cm}^{-1}$ ; it is worth noticing that in this system two Ti—O bond distances are obtained from X-ray diffraction, that is, 1.77 and 1.97 Å. In this case, the sequence along the chain is (Ti—O—Ti—O—Ti—O—Ti). The stretching frequency of the short Ti—O bond should be located, as suggested by Su et al.,<sup>18</sup> near 850  $\text{cm}^{-1}$  (this band is present in the Raman spectrum of  $\text{CaTiSiO}_5$ ), by analogy with the Raman spectrum of natasite ( $\text{Na}_2\text{TiSiO}_5$ ), where a similar short Ti—O bond is present. Notice that distortions, which characterize the  $\text{TiO}_6$  chains in  $\text{Na}_2\text{TiSi}_4\text{O}_{11}$  and  $\text{CaTiSiO}_5$ , are quite a half with respect to that proposed in ref 30 for ETS-10 (where  $\Delta(\text{Ti—O}) = 0.4$  Å).

For the sake of brevity, the discussion of the obtained results will be only centered on a selection of normal modes, which involve directly the  $\text{TiO}_6$  moiety. A schematic representation

of some of these modes and their corresponding frequencies are presented in Table 3. The distinction between IR (I) and Raman (R) active modes has been made on the basis of their symmetry with respect to the inversion center of the  $P2_1/m11$  used. Notice that the calculated frequencies have been scaled<sup>37</sup> by a factor 0.9, as well-established technique used to correct the HF frequencies.

As previously mentioned in the Optimized Models section, the absence of any negative frequencies indicates that the optimized structures correspond to minima. As can be seen from Table 3 (modes labeled as 1 and 2), positive frequencies (e.g., 186 and 561  $\text{cm}^{-1}$  for model II) are associated with normal modes causing ferroelectric distortion (i.e., off-centering of Ti atom from the equatorial plane). The same can be said for mode 5 (498  $\text{cm}^{-1}$  for model II), which would cause alternating short and long Ti—O<sub>ap</sub> distances along the chain. So both of these types of deformations are expected to be energetically unfavored, and this can justify the correctness of the chosen symmetry for

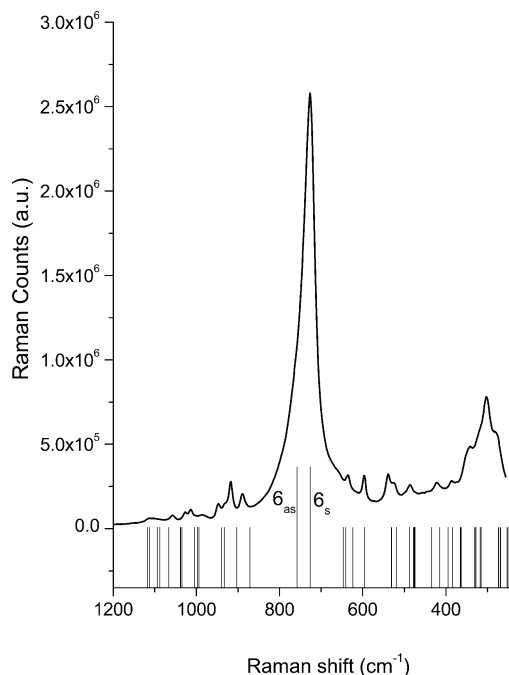


**Figure 4.** Comparison between the experimental Raman spectrum (full line, obtained with a 442 nm laser line with a Renishaw Micro-Raman System 1000), and that obtained on model II and scaled by a factor<sup>37</sup> of 0.9 (stick lines, the vibration modes at 758 and 726  $\text{cm}^{-1}$  have been highlighted).

**TABLE 3: Selected Calculated Vibrational Modes of Models I and II (Only the  $\text{TiO}_6$  Wire Is Represented)<sup>a</sup>**

Vibrational Mode		Model I	Model II
1		(I) 198	(I) 186
2		(I) 565	(I) 561
3		(I) 416	(I) 407
4		(R) 495	(R) 488
5		(I) 507	(I) 498
6		(R) 746	(R) 758 ( $6_{\text{as}}$ ) (R) 726 ( $6_{\text{s}}$ )
7		(R) 992	(R) 997
8		(R) 1042	(R) 1039

<sup>a</sup> The values are expressed in  $\text{cm}^{-1}$ . (I) and (R) indicate the infrared and Raman active modes, respectively. According to ref 37, the values in the table are obtained by scaling the computed HF values by a factor of 0.9.

the optimization procedure. Other type of deformations of the  $\text{TiO}_6$  moiety such as those represented by modes 3 and 4 have also positive frequency values, 407 and 488  $\text{cm}^{-1}$  when model II is considered.

As far as the vibrational modes coming from the Ti—O bond stretching, the determination of which represents one of the main scopes of this investigation, they give Raman active bands near 750  $\text{cm}^{-1}$  and in the 1050–800  $\text{cm}^{-1}$  spectral region. For the sake of brevity, in Table 3 only three of them are reported.

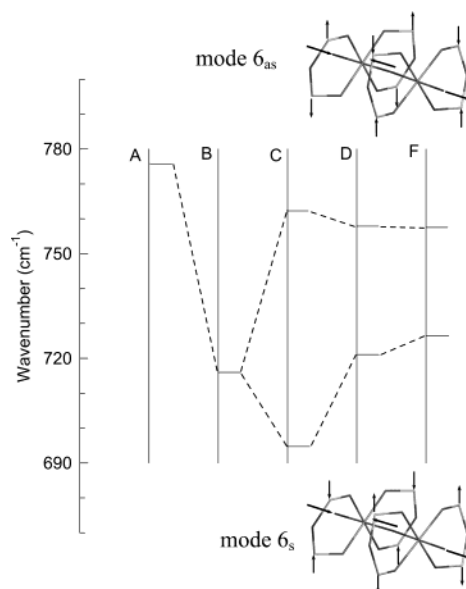


**Figure 5.** Analysis of the evolution of mode 6 in Table 3 on passing from fragments of increasing size (see the text for details). The atomic displacement of modes  $6_{\text{as}}$  and  $6_{\text{s}}$  are schematized in the up and down insets.

Concerning the 1050–800  $\text{cm}^{-1}$  range, a schematized representation of two modes, falling near 995 and 1040  $\text{cm}^{-1}$ , is reported in Table 3. Mode 7 can be considered as an out-of-phase combination along the Ti—O—Ti—O—Ti chain of the total-symmetric stretching of the  $\text{TiO}_6$  octahedra, while mode 8 is the corresponding in-phase combination. At variance with respect to mode 7, in mode 8 no contributions from the displacements of the  $\text{O}_{\text{ap}}$  along the Ti—O—Ti—O—Ti occurs; for this reason, mode 8 can be considered as a pure Ti— $\text{O}_{\text{eq}}$  stretching mode. Finally, no significant variations for modes 7 and 8 are observed on passing from model I to model II.

Coming now to the spectral region near the 726  $\text{cm}^{-1}$  Raman fingerprint, isolated vibrational modes (labeled as 6 in Table 3) are obtained. They are associated with frequencies that are centered at 746  $\text{cm}^{-1}$  (model I) and at 726 (hereafter  $6_{\text{s}}$ ) and 758 (hereafter  $6_{\text{as}}$ )  $\text{cm}^{-1}$  (model II). As can be seen from Table 3, mode 6 consists principally of an out-of-phase combination along the Ti—O—Ti—O—Ti chain of the stretching of the two Ti— $\text{O}_{\text{ap}}$  bonds in the  $\text{O}_{\text{ap}}$ —Ti— $\text{O}_{\text{ap}}$  moiety. The analysis of the associated displacement vectors shows that significant contributions neither from the equatorial oxygen atoms nor from Ti are present and that  $\text{O}_{\text{ap}}$  are displaced from their equilibrium position along the  $x$  direction only. On passing from model I to II, this mode results to be split into two components, at 758 and 726  $\text{cm}^{-1}$ . We have observed that this effect is due to a weak coupling (758 asymmetric, 726 symmetric,  $\Delta\nu = 32 \text{ cm}^{-1}$ ) with a symmetric stretching of the Si—O—Si moiety in the three-membered ring, as it is schematized in Figure 5. Since mode  $6_{\text{as}}$  is coming from an asymmetric coupling, it can be expected that its Raman intensity would be lower than that of mode  $6_{\text{s}}$ . The 725  $\text{cm}^{-1}$  fingerprint band is the  $6_{\text{s}}$  symmetric mode, and the tail in the high-frequency side is the contribution of the weaker  $6_{\text{as}}$  mode. The good agreement between the experimental<sup>18–20</sup> spectrum and the results obtained for model II is noteworthy, both in the prediction of the position and symmetry (Raman active) and in exploiting the shape (presence of a shoulder on the high  $\nu$  side). In conclusion, the assignment of the intense band observed in the Raman spectrum of ETS-10<sup>18–20</sup> can be effectively considered as a fingerprint of the material, since it is the combination of Ti— $\text{O}_{\text{ap}}$  stretches along



the corner-sharing  $\text{TiO}_6$  chains without a direct participation of the equatorial oxygen atoms. The same conclusion was already suggested by Su et al.<sup>18</sup>

To shed additional light on the attribution of mode 6, we have exploited a recently developed utility of the upgraded version of the CRYSTAL code that allows the calculations of the vibrational modes to be performed on selected “atomic fragments” of the unit cell, while maintaining the periodic boundary conditions. Normal modes are thus obtained by decoupling the atomic fragment vibrational motions from the rest of the structure. The results of this analysis, performed on model II, are presented in Figure 5. In this figure, the calculated frequencies (scaled by a factor 0.9)<sup>37</sup> for mode 6 on fragments A–F are presented. In fragment A, only Ti and  $\text{O}_{\text{ap}}$  atoms are included in the calculation of the frequency; in fragment B, besides the atoms considered in fragment A, the  $\text{O}_{\text{eq}}$  atoms are added; in fragment C, the silicon atoms bonded to  $\text{O}_{\text{eq}}$  are further considered; in fragment D, also the O atoms that complete the three-membered ring and the O atom that constitutes the basis of the five-membered ring (see Figure 1, part c) are considered; finally, in the fragment labeled F, all of the atoms of the unit cell (values reported in Table 3 and commented above) are considered. Obviously the values of F are the best computed values (reference values) of this work.

Fragment A presents a single Raman active band centered at  $776\text{ cm}^{-1}$  that represents an overestimation of about 5% with respect to the center of mass of the values obtained with F. This result indicates that both modes  $6_{\text{as}}$  and  $6_{\text{s}}$  can be assigned to normal vibrations mainly involving the Ti– $\text{O}_{\text{ap}}$  bond stretches of the chain. However, this small fragment is not able to reproduce the splitting of mode 6 in  $6_{\text{as}}$  and  $6_{\text{s}}$  obtained on F. The same can be said for fragment B. In this case, an underestimation of about 4% is obtained. Moreover, the analysis of the atomic displacements constituting the normal mode indicates that it is not a pure Ti– $\text{O}_{\text{ap}}$  stretching and that a contribution from the  $\text{O}_{\text{eq}}$  atoms plays not a negligible role unlike in F calculation.

From the comparison of the data of fragment C and F, it turns out that at least the first neighbor Si atoms have to be included in the calculation to obtain the coupling observed in F. The value obtained for this splitting ( $\Delta\nu = 67\text{ cm}^{-1}$ ) is significantly larger than that calculated for F ( $\Delta\nu = 32\text{ cm}^{-1}$ ); this can be explained by considering that Si atoms are dangling in fragment C. The computed center of mass of the two bands is now considerably closer to that obtained on F. Finally, comparing the normal-mode analysis of B and C, it is concluded that the contribution from  $\text{O}_{\text{eq}}$  falls down on passing from B to C, so that it can be again considered as a mode (mainly) localized along the Ti–O–Ti–O–Ti chain. The same considerations hold for fragment D, but in this case, the agreement with the F results is obviously increased.

From all these considerations, it is concluded that, once the Ti–O–Ti–O–Ti chain is properly embedded into a siliceous matrix, the Raman active  $726\text{ cm}^{-1}$  fingerprint band can be definitely assigned to a normal mode basically involving the Ti– $\text{O}_{\text{ap}}$  stretches.

## Conclusions

In this work, periodic ab initio calculations on the electronic and vibrational properties of the ETS-10 system have been reported. The results so obtained are comparable with experimental data (DRUV–vis and Raman spectroscopies). This complex material was modeled by adopting monodimensional periodic models (namely, models I and II), constructed around

the Ti–O–Ti–O chain. Unlike previous models,<sup>8</sup> in this work positive counterions have been considered, so all of the electrons that are expected to be present from stoichiometry of the real material have been considered. Both cell parameter and internal atomic coordinates have been fully optimized, thus ensuring that the minimum energy geometry for the adopted basis set and Hamiltonian (HF) is reached. The optimized structures well agree with the experimental geometry coming from single-crystal X-ray diffraction.<sup>4</sup> The analysis of DOSs obtained at HF, B3LYP, and LDA-VWN levels (the last two calculations performed on the HF-optimized structure) shows that states coming from apical oxygen atoms of the  $\text{TiO}_6$  octahedra span a narrow energy range (about 0.5–0.6 eV). The values for  $E_{\text{g}}$  evaluated as the difference between the top of the VB and the bottom of the CB follow the expected trend:<sup>32,33</sup> HF  $\gg$  B3LYP  $>$  LDA-VWN.

The main results derived from the analysis of the normal modes computed at HF level on the full cell and on fragments of increasing size can be summarized as follows. The Raman fingerprint (found experimentally at  $725\text{ cm}^{-1}$ , see Figure 4)<sup>18–20</sup> is mainly due to a symmetric combination of Ti– $\text{O}_{\text{ap}}$  stretches along the chain; this mode is slightly split in two components as a consequence of its combination with the stretching of the Si–O–Si moiety. The analysis of “atomic fragments” of increasing complexity allowed us to conclude that this effect is due to the embedding of the Ti–O–Ti–O chains in the siliceous matrix.

Finally, periodic ab initio calculation of harmonic vibrational frequencies, as implemented in the CRYSTAL code, has been demonstrated to be a powerful tool to characterize complex materials as zeolites and thus fully support experimental investigations.

**Acknowledgment.** The Secretaría de Estado de Educación y Universidades of Spain is gratefully acknowledged for a postdoctoral grant to F.X.L.X. The MIUR-COFIN00, Compagnia San Paolo di Torino, and Fondazione CRT di Torino are gratefully acknowledged for financial supports. C.M.Z.W. acknowledges support from SEP-FOMES2000 through Project “Cómputo científico” for unlimited CPU time on the IBM-p690 32-processor supercomputer at UAEM. We are also indebted with Prof. R. Dovesi of the Theoretical Chemistry Group in Turin for fruitful discussions.

**Supporting Information Available:** The detailed description of the whole procedure adopted to optimize models I and II (*a* cell parameter plus internal atomic coordinates), together with a figure schematizing the optimization process for model I, and the description of the vibrational modes calculation. This material is available free of charge via the Internet at <http://pubs.acs.org>.

## References and Notes

- (1) Kuznicki, S. M. U.S. Patent 4,853,202, 1989.
- (2) Anderson, M. W.; Terasaki, O.; Oshuna, T.; Philippou, A.; Mackay, S. P.; Ferreira, A.; Rocha, J.; Lidin, S. *Nature* **1994**, *367*, 347–351.
- (3) Anderson, M. W.; Terasaki, O.; Oshuna, T.; O'Malley, P. J.; Philippou, A.; Mackay, S. P.; Ferreira, A.; Rocha, J.; Lidin, S. *Philos. Mag. B* **1995**, *71*, 813–841.
- (4) Wang, X.; Jacobson, A. J. *Chem. Commun.* **1999**, 973–974.
- (5) Kuznicki, S. M.; Thrush, K. A.; Allen, F. M.; Levine, S. M.; Hamil, M. M.; Hayhurst, D. T.; Mansour, M. In *Molecular Sieves. Synthesis of Microporous Materials*; Occelli, M. L., Robson, H. E., Eds.; Van Nostrand Reinhold: New York, 1992; Vol. I, Chapter 29.
- (6) Borello, E.; Lamberti, C.; Bordiga, S.; Zecchina, A.; Otero Areán, C. *Appl. Phys. Lett.* **1997**, *71*, 2319–2321.
- (7) Lamberti, C. *Microporous Mesoporous Mater.* **1999**, *30*, 155–163.



- (8) Bordiga, S.; Turnes Palomino, G.; Zecchina, A.; Ranghino, G.; Giamello, E.; Lamberti, C. *J. Chem. Phys.* **2000**, *112*, 3859–3867.
- (9) Cui, Y.; Lieber, C. M. *Science* **2001**, *291*, 851–853.
- (10) Duan, X. F.; Huang, Y.; Cui, Y.; Wuang, J. F.; Lieber, C. M. *Nature* **2001**, *409*, 66–69.
- (11) Cui, Y.; Wei, Q. Q.; Park, H. K.; Lieber, C. M. *Science* **2001**, *293*, 1289–1292.
- (12) Huang, Y.; Duan, X. F.; Cui, Y.; Lauhon, L. J.; Kim, K. H.; Lieber, C. M. *Science* **2001**, *294*, 1313–1317.
- (13) Fox, M. A.; Doan, K. E.; Dulay, M. T. *Res. Chem. Intermed.* **1994**, *20*, 711–722.
- (14) Calza, P.; Pazè, C.; Pelizzetti, E.; Zecchina, A. *Chem. Commun.* **2001**, 2130–2131.
- (15) Howe, R. F.; Krisnandi, Y. K. *Chem. Commun.* **2001**, 1588–1589.
- (16) Llabrés i Xamena, F. X.; Calza, P.; Lamberti, C.; Prestipino, C.; Damin, A.; Bordiga, S.; Pelizzetti, E.; Zecchina, A. *J. Am. Chem. Soc.* **2003**, *125*, 2264–2271.
- (17) Krisnandi, Y. K.; Southon, P. D.; Adesina, A. A.; Howe, R. F. *Int. J. Photoenergy* **2003**, *5*, 131–140.
- (18) Su, Y.; Balmer, M. L.; Bunker, B. C. *J. Phys. Chem. B* **2000**, *104*, 8160–8169.
- (19) Southon, P. D.; Howe, R. F. *Chem. Mater.* **2002**, *14*, 4209–4218.
- (20) Llabrés i Xamena, F. X.; Damin, A.; Bordiga, S.; Zecchina, A. *Chem. Commun.* **2003**, 1514–1515.
- (21) de Man, A. J. M.; Sauer, J. J. *J. Phys. Chem.* **1996**, *100*, 5025–5034.
- (22) Ching, W. Y.; Xu, Y.-N.; Gu, Z.-Q. *Phys. Rev. B* **1996**, *54*, 15585–15588.
- (23) (a) Saunders, V. R.; Dovesi, R.; Roetti, C.; Causà, M.; Harrison, N. M.; Orlando, R.; Zicovich-Wilson, C. M. *CRYSTAL-98 User's manual*; Università di Torino: Torino, Italy, 1999. (b) Doll, K. *Comput. Phys. Commun.* **2001**, *137*, 74–88. (c) Civalleri, B.; D'Arco, Ph.; Orlando, R.; Saunders, V. R.; Dovesi, R. *Chem. Phys. Lett.* **2001**, *348*, 131–138. (d) Doll, K.; Saunders, V. R.; Harrison, N. M. *Int. J. Quantum Chem.* **2001**, *82*, 1–13.
- (24) Schlegel, H. B. *J. Comput. Chem.* **1982**, *3*, 214–218.
- (25) Damin, A.; Bordiga, S.; Zecchina, A.; Doll, K.; Lamberti, C. *J. Chem. Phys.* **2003**, *118*, 10183–10194.
- (26) Becke, A. D. *J. Chem. Phys.* **1993**, *98*, 5648–5652.
- (27) Lee, C.; Yang, W.; Parr, R. G. *Phys. Rev. B* **1988**, *37*, 785–789.
- (28) Zicovich-Wilson, C. M.; Dovesi, R. *J. Phys. Chem. B* **1998**, *102*, 1411–1417.
- (29) Prencipe, M.; Zupan, A.; Dovesi, R.; Aprà, E.; Saunders, V. R. *Phys. Rev. B* **1995**, *51*, 3391–3396.
- (30) Sankar, G.; Bell, R. G.; Thomas, J. M.; Anderson, M. W.; Wright, P. A.; Rocha, J. J. *J. Phys. Chem.* **1996**, *100*, 449–452.
- (31) Grillo, M. E.; Carrazza, J. J. *J. Phys. Chem.* **1996**, *100*, 12261–12264.
- (32) Harrison, N. M. *Comput. Phys. Commun.* **2001**, *137*, 59–73.
- (33) Muscat, J.; Wander, A.; Harrison, N. M. *Chem. Phys. Lett.* **2001**, *342*, 397–401.
- (34) Dirac, P. A. M. *Proc. Cambridge Philos. Soc.* **1930**, *26*, 376–385.
- (35) Vosko, S. H.; Wilk, L.; Nusair, N. *Can. J. Phys.* **1980**, *58*, 1200–1211.
- (36) Damin, A. et al., manuscript in preparation.
- (37) Scott, A. P.; Radom, L. *J. Phys. Chem.* **1996**, *100*, 16502–16513.